Scalar power spectra and turbulent scalar length scales of high-Schmidt-number passive scalar fields in turbulent boundary layers

Mohammad Mohaghar,[1,*] Lakshmi P. Dasi,[1,2] and Donald R. Webster[1]
[1]*School of Civil and Environmental Engineering, Georgia Institute of Technology, 790 Atlantic Drive, Atlanta, Georgia 30332, USA*
[2]*Coulter Department of Biomedical Engineering, Georgia Institute of Technology, 313 Ferst Drive, Atlanta, Georgia 30332, USA*

(Received 27 February 2020; accepted 27 July 2020; published 10 August 2020)

This experimental study investigates the effects of Reynolds number ($5000 \leqslant \mathrm{Re} \leqslant 20000$, where $\mathrm{Re} = UH/\nu$) and initial release diameter ($2.2\ \mathrm{mm} \leqslant D \leqslant 9.4\ \mathrm{mm}$) on the scalar power spectra, fractal geometry, and turbulent length scales of high-Schmidt-number passive scalar fields resulting from an isokinetic release in a turbulent boundary layer. The turbulence analysis is based on 12 000 scalar fields collected using the planar laser-induced fluorescence technique for each case at six locations downstream. The scalar integral length scale and scalar Taylor microscale are calculated directly from the fields using the autocorrelation function and variance/gradient of the concentration fluctuation fields. With increasing downstream distance, the Taylor microscale decreases and the integral length scale increases, each to an asymptotic value. This indicates a larger range of scales exists as the scalar becomes more mixed, as one would expect. For locations beyond $x/H \geqslant 10$ (where H is the flow depth), the self-similarity condition is observed by considering the ratio between the scalar integral length scale and scalar Taylor microscale. Local isotropy is approached as measured by computing the ratio of longitudinal to transverse scalar Taylor microscales, and a change in the growth rate is observed for the fractal dimension computed from a planar section of the interfaces in the concentration fluctuation fields. The spectral slope magnitude in the inertial-convective regime decreases near the source ($x/H < 10$) due to the large-scale anisotropy. In the self-similar regime ($x/H \geqslant 10$), the scaling-exponent is found to be dependent on the initial release diameter. The lower wave-number portion of the inertial-convective regime, where the scales are larger than or closer to the scale of the nozzle diameter, scales close to k^{-1} scaling in agreement with the cascade-bypass situation, and the spectral slope in the upper wave-number portion of the inertial-convective regime is found to be closer to $-5/3$. The viscous-convective scaling behavior deviated significantly from Batchelor's k^{-1} scaling law, clearly disputing the generality of Batchelor's arguments. Intermittency analysis, using computation of the intermittency factor as well as probability density functions of the fluctuating scalar gradient, suggests that the discrepancy between theory and observations for the scaling of the viscous-convective regime can be explained by the high intermittency in the small scales of the scalar fluctuations.

DOI: 10.1103/PhysRevFluids.5.084606

I. INTRODUCTION

When addressing turbulent scalar mixing applications, the scalar power spectra provides important information regarding the range of scales in the flow. The main theory for prediction of scaling

*mohaghar@gatech.edu

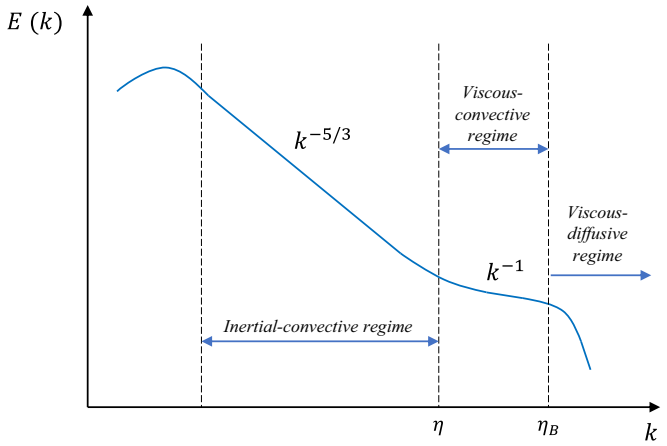

FIG. 1. Conceptual schematic of the spectrum for a locally isotropic fluctuating passive scalar field for $\mathrm{Sc} \gg 1$, shown on log axes.

in the inertial-convective regime (i.e., $1/L \ll k \ll 1/\eta$, where k is the wave number, L is the integral length scale, and η is the Kolmogorov length scale) of scalar power spectra was originally introduced by Oboukhov [1] and Corrsin [2]. The passive scalar structure in the inertial-convective regime is hypothesized to be a function of dissipation rate of the scalar fluctuations, χ, and energy dissipation rate, ε, only, and the scalar power spectrum takes the form $E(k) = C_s \chi \varepsilon^{-1/3} k^{-5/3}$, where C_s is the Obukhov-Corrsin universal constant [3,4]. This prediction is analogous to the 1941 Kolmogorov theory, where the energy spectrum is predicted to be proportional to $k^{-5/3}$ in the inertial regime, and the Obukhov-Corrsin length scale, $\eta_{oc} = (\kappa^3/\varepsilon)^{1/4}$, is analogous to the Kolmogorov length scale, where κ is the scalar diffusivity [5].

Batchelor [6] and Batchelor *et al.* [7] recognized that the cutoff length scale, η_{oc}, is appropriate only for low Schmidt number passive scalars ($\mathrm{Sc} \leqslant 1$) and that the strain rate of the fluctuating velocity field determines the cutoff length scale for scalars with high Schmidt numbers ($\mathrm{Sc} \gg 1$). Using dimensional reasoning, a new length scale for the cut-off point was put forward as $\eta_B = (\nu\kappa^2/\varepsilon)^{1/4}$, which is now called the Batchelor length scale, and can be expressed in terms of the Kolmogorov length scale as $\eta_B = \eta \mathrm{Sc}^{-1/2}$. Batchelor [6] derived the behavior of the passive scalar spectrum for $k \gg 1/\eta$ as $E(k) = q\langle\chi\rangle(\nu/\langle\varepsilon\rangle)^{1/2}k^{-1}\exp[-q(k\eta_B)^2]$, where q is a dimensionless constant. Thus, the spectrum scales as k^{-1} in the viscous-convective regime ($1/\eta \ll k \ll 1/\eta_B$). Kraichnan [8] modified this formula to take into account the stochastic nature of the fluctuating strain rate. The modified formula by Kraichnan [8] also predicts k^{-1} scaling in the viscous-convective regime, but it changes the constant in the exponential function. A schematic of the passive scalar spectrum with the scaling at different regions for $\mathrm{Sc} \gg 1$ is shown in Fig. 1.

Although several experimental and computational studies have investigated the validity of the theories for the scaling of the inertial-convective and viscous-convective regimes in the scalar power spectrum, there are still debates and discussions about refinements of these theories. Several studies reported that the spectral slope in the inertial-convective regime of scalar spectra is close to $-5/3$ (closer in the case of shearless flows) and appears to approach $-5/3$ with increasing Reynolds number [9–14]. However, less agreement has been achieved regarding Batchelor's k^{-1} scaling prediction for the viscous-convective regime for the case of high Schmidt number passive scalars. Following Batchelor's prediction [6], laboratory measurements by Gibson and Schwarz [15], measurements in the ocean by Grant *et al.* [16], and direct numerical simulation by Yeung *et al.* [13] reported agreement with the k^{-1} scaling law. In contrast to these observations, Gargett [17] found no evidence of the -1 slope in her measurements in the ocean. Similarly, scalar mixing measurements reported in shear layers [18], turbulent jets [19], and magnetically forced

FIG. 2. Dye visualization of the plume at Re = 10 000 with a nozzle diameter of 4.7 mm.

two-dimensional turbulence [20] lacked the k^{-1} scaling regime. Nevertheless, in a review article, Warhaft [10] argued that there is persuasive evidence for the existence of the k^{-1} scaling based on the theory of Kraichnan [8] and Holzer and Siggia [21]. Clearly, careful experiments must be conducted to address this issue.

Further, turbulent length scales in the passive scalar fields provide insight about the range of scales, self-similarity, and local isotropy in the flow. The scalar Taylor microscale is the important characteristic length scale [22–24]. Analysis of turbulent length scales near the edge of a shear layer at low Schmidt number revealed that the scalar Taylor microscale is close to the scale of the jumps in the scalar gradient profiles [25]. Additionally, it was found that the relationship between the scalar integral length scale and scalar Taylor microscale (constant ratio) is an indication of self-similarity in the flow [26]. The scalar integral length scale, and its relation to the scalar Taylor microscale, are important to understand the process of scalar fluctuation production and dissipation rate by measuring the correlation of scalar fluctuations between two points in the flow [27–35].

The present work studies the effects of Reynolds number ($5\,000 \leqslant \mathrm{Re} \leqslant 20\,000$) and initial scalar release diameter (2.2 mm $\leqslant D \leqslant$ 9.4 mm) on the scaling of power spectra using high resolution planar laser-induced fluorescence (PLIF) measurements of high Schmidt number passive scalar fields in turbulent boundary layers. Scalar plumes are of interest for applications, such as point source release of pollutants and other chemicals [36], and further provide an opportunity to examine universal turbulent characteristics. Local isotropy, self-similarity, range of scales, and the flow status are analyzed by measuring the scalar length scales and fractal dimension. The following sections describe the experimental procedures employed in our work and discuss and interpret the data via the scalar length scales, the fractal dimension analysis of the scalar variance, the intermittency, and the scalar power spectra.

II. EXPERIMENTAL PROCEDURE

The important experimental details are described briefly here since more details of the methods are provided in previous studies [37,38]. Experimental measurements of the scalar field in a high Schmidt number passive scalar plume (Sc $\approx$ 1000) released at mid-depth within a turbulent boundary layer in an open channel flow are collected at 6 downstream distances from the source: H, $2.5H$, $5H$, $10H$, $20H$, and $40H$, where $H = 100$ mm is the flow depth. The turbulent boundary layer develops over a smooth surface in a wide rectangular channel, and it was fully developed at the measurement location and hence not evolving in the streamwise direction (Fig. 2). To minimize the wake perturbation, each nozzle was custom-built with a streamlined fairing. The local mean velocity in the boundary layer and the source velocity is matched, which leads to isokinetic nozzle release of the Rhodamine 6G solution. To investigate effects of both Reynolds number and initial release diameter (length scale), experiments were performed for three Reynolds numbers of 5 000, 10 000, and 20 000, and three inner orifice diameters of 2.2, 4.7, and 9.4 mm.

Figure 3 shows the schematic of the experimental setup for the high-resolution PLIF technique used to measure 12 000 passive scalar fields at each location for each Reynolds number and nozzle diameter. The beam waist for PLIF measurement is created in a way to be smaller than the Kolmogorov length scale and on the order of the Batchelor length scale (waist diameter is 80 μm at an elevation of the mid-depth of the flow). The midrange of the viscous-convective regime is resolved based on the beam waist diameter. Thus, the size of beam waist diameter has a minimal effect on the power spectra [37,38].

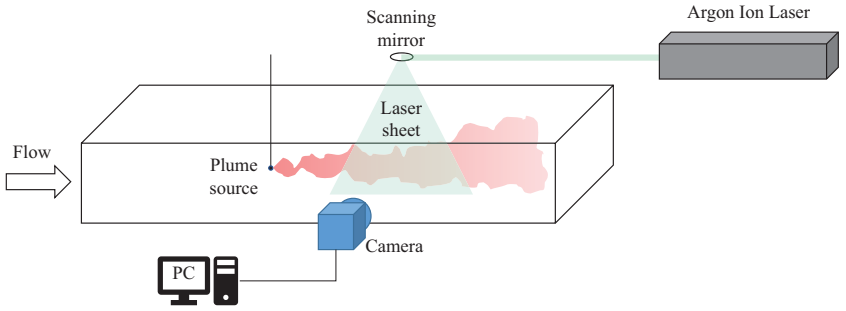

FIG. 3. Schematic of the experiment setup for concentration measurements via PLIF.

Estimations of the velocity length scales, Reynolds numbers based on the outer-scale (largest scale), and Taylor-scale eddies are reported in Table I. The details of the velocity measurements, which were obtained using particle tracking velocimetry (PTV) technique, are reported in Dasi [38]. The characteristic velocity scale for turbulence is the root mean square of the velocity fluctuations, $u' = \sqrt{\overline{u_i' u_i'}/2}$. The estimation of the Taylor microscale in the flow under the assumption of isotropic turbulence can be found using $\lambda \approx (15\nu u'^2/\varepsilon)^{1/2}$, where ν is kinematic viscosity. The Reynolds numbers based on the largest scales, Taylor microscale, and friction velocity (u^*) are defined as $\mathrm{Re} = UH/\nu$, $\mathrm{Re}_\lambda = u'\lambda/\nu$, and $\mathrm{Re}_\tau = u^* H/\nu$, respectively. Using equilibrium turbulence arguments, the energy dissipation rate can be re-expressed as $\varepsilon \approx \frac{u'^3}{H/2}$, where $H/2$ is the approximate length-scale of the largest eddies [39–41]. The Kolmogorov length scale and the Batchelor length scale are estimated as $\eta \approx (\nu^3/\varepsilon)^{1/4}$ and $\eta_B \approx \eta \mathrm{Sc}^{-1/2}$, respectively [39]. The 12-bit CCD camera with 1392×1024 pixels and a 200-mm macrolens were used for image capturing. The PLIF image resolution is approximately 13 μm/pixel, which roughly matches the Batchelor length scale.

III. RESULTS AND DISCUSSION

The scalar turbulent length scales, fractal dimension, intermittency, and scaling of the scalar spectra are analyzed based on the concentration variance (fluctuation). The concentration fluctuation is computed using the decomposition of scalar fields into mean and fluctuating components, $C' = C - \langle C \rangle$, where $\langle C \rangle$ is the ensemble average of concentration fields. Thus, it is important to first analyze the variation of the concentration average along the downstream distance. The concentration fields are extracted from corrected PLIF images and the details of image correction based on the source concentration were previously discussed by Dasi *et al.* [37], Dasi [38], Webster *et al.* [42], Rahman and Webster [43].

Figures 4(a) and 4(b) show the variation of the ensemble averaged concentration normalized by the source concentration along the plume centerline for three different Reynolds numbers and three different nozzle diameters, respectively. It was shown by Webster *et al.* [42] that for $x/H > 2$,

TABLE I. Experimental parameters and typical length scales.

Re	u'(mms^{-1})	u^*(mms^{-1})	Re_λ	Re_τ	ε(m^{2}s^{-3})	λ(mm)	η(mm)	η_B(mm)	D(mm)	D/η
5 000	5.3	3.25	60	325	3×10^{-6}	11	0.76	0.024	4.7	6.2
									2.2	5.2
10 000	11.8	6.4	90	640	3.3×10^{-5}	8	0.42	0.013	4.7	11.2
									9.4	22.4
20 000	19.1	10.6	120	1060	1.4×10^{-4}	6	0.29	0.009	4.7	16.2

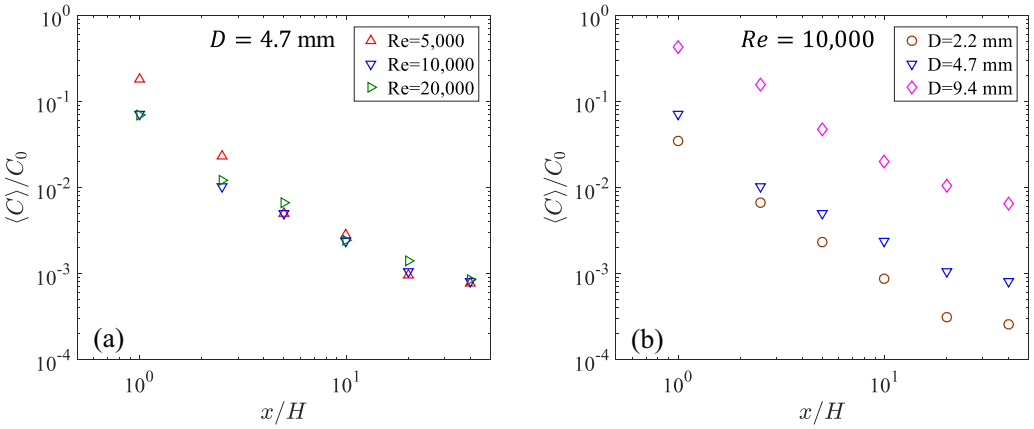

FIG. 4. Evolution of the average scalar concentration as a function of (a) Reynolds number and (b) source nozzle diameter.

where the eddy diffusivity is constant, the average concentration varies inversely with the distance from the source, which is in agreement with the theoretical model [44]. However, the decrease is faster for all experimental cases near the source $x/H < 2$ where the eddy diffusion coefficient is not constant [38,42]. In addition, although the normalized ensemble-averaged concentration shows minimal variation among different Reynolds numbers for the same release diameter [Fig. 4(a)], the ratio increases by increasing initial release diameter and maintaining the same Reynolds number [Fig. 4(b)].

A. Turbulent scalar length scales

Direct information on the turbulent scalar length scales provides insight to the turbulent flow dynamics and morphology. Two main methods of computing the scalar length scales directly from the fluctuating scalar fields are discussed in this study to investigate the temporal evolution of the length scales, self-similarity, and local isotropy in the flow. The first method is to use the spatial autocorrelation function, which measures the influence of the turbulent scalar fluctuations at neighboring points, to calculate both the scalar integral and scalar Taylor length scales. Defining the scalar integral scale in turbulent flow is important to understand the process of variance production and dissipation rate, and the integral length scale can be defined as the distance of the correlation between two points in the flow [45]. The integral length scale of the scalar fluctuation field is defined as

$$L = \int f(r)dr, \tag{1}$$

where r is the distance between two points in the flow, and $f(r)$ is the scalar fluctuation autocorrelation function, which is computed using

$$f(r) = \frac{\langle C'(x)C'(x+r)\rangle}{\langle (C')^2\rangle}. \tag{2}$$

The first terms in the Taylor series of the autocorrelation function can be derived as

$$f(r) = 1 + \frac{1}{2}\frac{d^2 f(0)}{dr^2}r^2 = 1 - \frac{r^2}{\lambda_T^2}, \tag{3}$$

where λ_T is the scalar Taylor microscale [39]. This scale is the intermediate length scale in which turbulent filaments are affected by molecular diffusion, and it can be calculated from a parabola

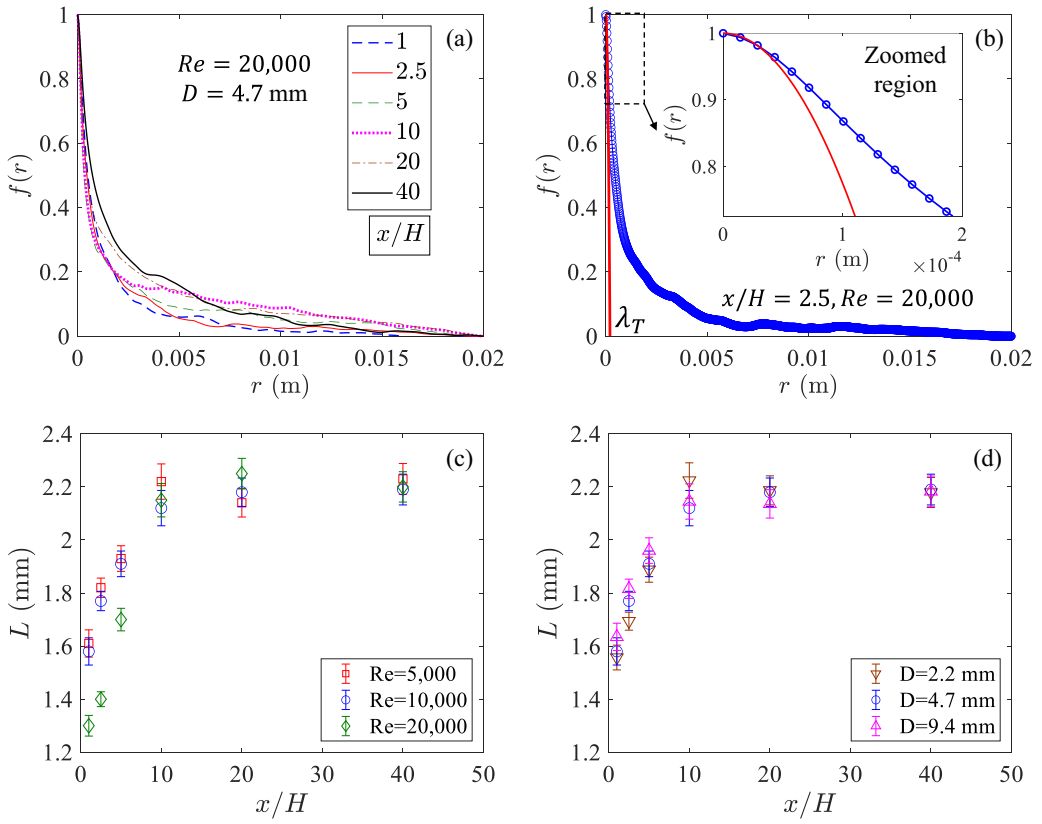

FIG. 5. (a) The ensemble average of the longitudinal autocorrelation function of concentration fluctuations for Re = 20 000 and $D = 4.7$ mm. (b) The ensemble average of the longitudinal autocorrelation function of the concentration fluctuations at $x/H = 2.5$ and Re = 20 000, and zoomed region of the fitted line to the first three points for clarity. Evolution of the scalar integral length scale calculated from the longitudinal autocorrelation functions as a function of (c) Reynolds number and (d) source nozzle diameter.

fitted to the curve of the autocorrelation function [34,35,46] using

$$\lambda_T = \left[-\frac{1}{2} \frac{d^2 f(0)}{dr^2} \right]^{-1/2}. \tag{4}$$

Figure 5(a) shows the evolution of the ensemble average of the longitudinal autocorrelation function for Re = 20 000. It indicates that the area under the autocorrelation function increases at $x/H < 10$, and hence the integral length scale increases with increasing x/H. In addition, it clarifies that the field of view is large enough for the autocorrelation function to decay to zero, and the integral length scale calculation to converge. The ensemble average of the longitudinal autocorrelation function of concentration fluctuations at $x/H = 2.5$ and Re = 20 000, and a zoomed region close to $f(r) = 1$, is shown in Fig. 5(b). The zoomed region shows the parabola fit to the first three data points of the autocorrelation function, and the scalar Taylor microscale is defined where the parabola fit crosses $f(r) = 0$. Figures 5(c) and 5(d) show the evolution of the scalar integral length scale as a function of distance from the source. The scalar integral length scale grows in all cases for $x/H < 10$, and then it reaches an asymptotic value of roughly 2.2 mm. The growth trend of the scalar integral length scale is similar for all Reynolds numbers and nozzle diameters, although the Re = 20 000 case starts at a smaller integral length scale compared to the other cases.

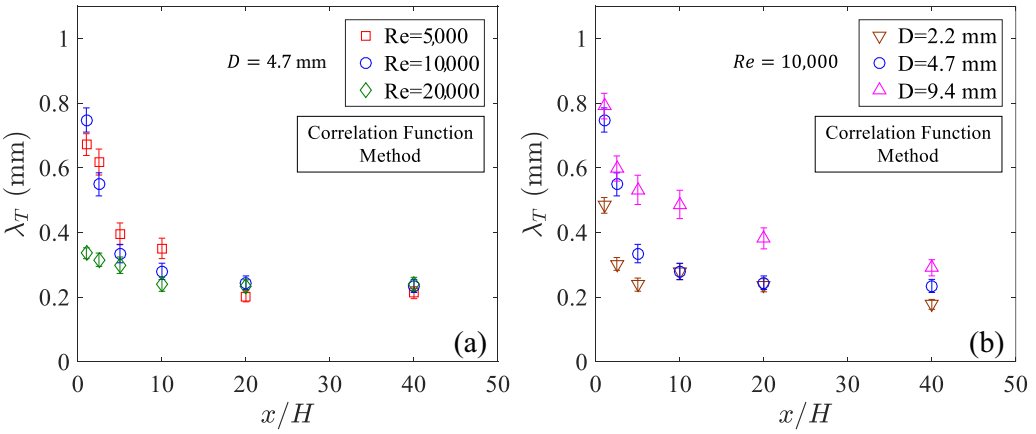

FIG. 6. Evolution of the scalar Taylor microscale calculated from the longitudinal autocorrelation function as a function of (a) Reynolds number and (b) source nozzle diameter.

Figures 6(a) and 6(b) show the effects of Reynolds number and initial nozzle diameter on the longitudinal scalar Taylor microscale. Unlike the growth trend in the scalar integral length scale, the scalar Taylor microscale decreases between $1 < x/H < 10$. However, similar to the integral length scale, this scale approaches an asymptotic value after $x/H = 10$. The scalar Taylor microscale, similar to the scalar integral length scale, starts with a smaller value at the highest Reynolds number (Re = 20 000), although the asymptotic value is almost the same as the other Reynolds number cases. Also, the scalar Taylor microscale for $x/H < 10$ is directly influenced by the initial nozzle diameter as seen in Fig. 6(b). In addition, the increasing ratio of L/λ_T farther downstream in the flow between $1 < x/H < 10$ verifies the increasing separation of scales. Another important finding is that the approximate constant ratio between the scalar integral length scale and the scalar Taylor microscale for $x/H \geqslant 10$ supports the existence of self-similarity in the scalar field in this region.

An alternative method of calculating the scalar Taylor microscale is used to investigate local isotropy in the scalar field. The scalar Taylor microscale calculated via the variance and gradient of the concentration fluctuations is defined by [22,47,48]

$$\lambda_{T_{\text{lon}}} = \sqrt{\frac{2\langle (C')^2 \rangle}{\left\langle \left(\frac{\partial C'}{\partial x}\right)^2 \right\rangle}}, \tag{5}$$

$$\lambda_{T_{\text{tran}}} = \sqrt{\frac{2\langle (C')^2 \rangle}{\left\langle \left(\frac{\partial C'}{\partial y}\right)^2 \right\rangle}}. \tag{6}$$

The longitudinal and transverse scalar Taylor microscales are shown in Figs. 7(a)–7(d). The magnitude, trend, and the asymptotic values of the Taylor microscales in the longitudinal direction at $x/H \geqslant 10$ based on this method are similar to the autocorrelation function method (discussed above). Prior to reaching to an asymptotic value ($x/H < 10$), the longitudinal and transverse scalar Taylor microscales decrease with increasing Reynolds number and with decreasing initial release diameter. This indicates that faster separation of scales and a wider range of scales occur in the scalar field at higher Reynolds number.

The analysis of local isotropy in the scalar field is shown in Fig. 8. The requirement for local isotropy is that the components of the dissipation rate of the scalar fluctuations should be

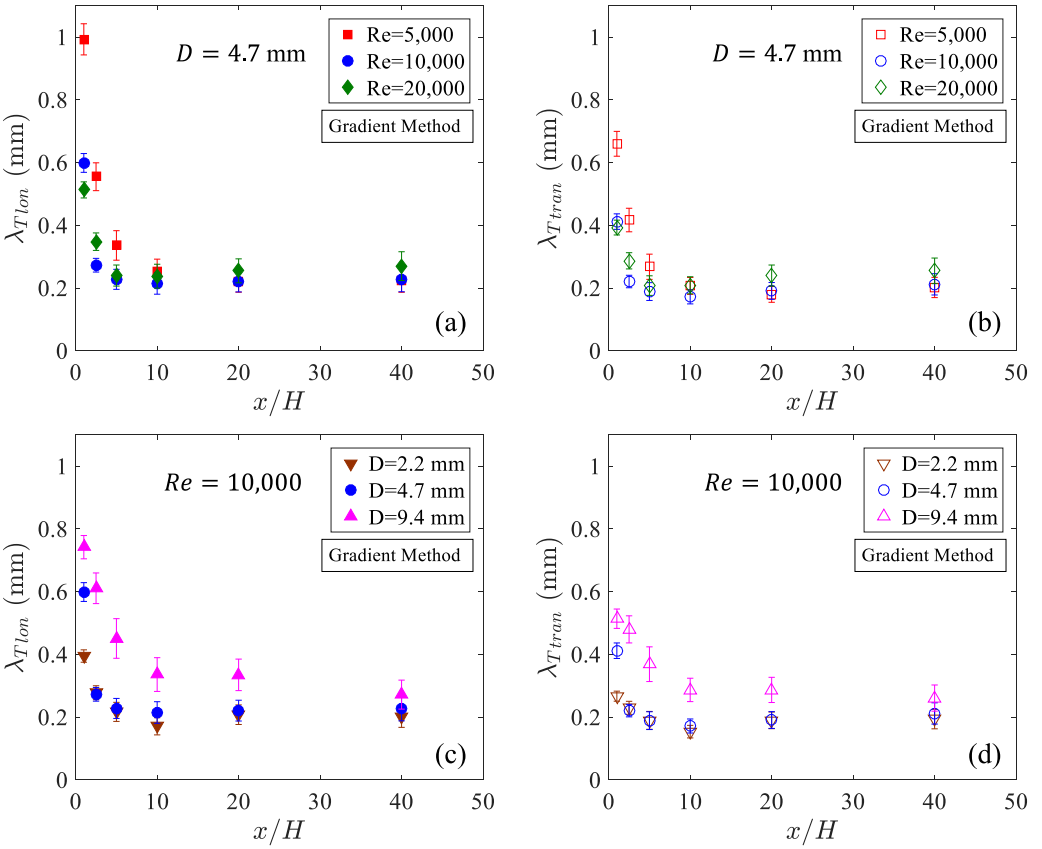

FIG. 7. Evolution of (a), (c) longitudinal and (b), (d) transverse scalar Taylor microscales calculated from the spatial gradient of the concentration fluctuations as a function of (a), (b) Reynolds number and (c), (d) source nozzle diameter.

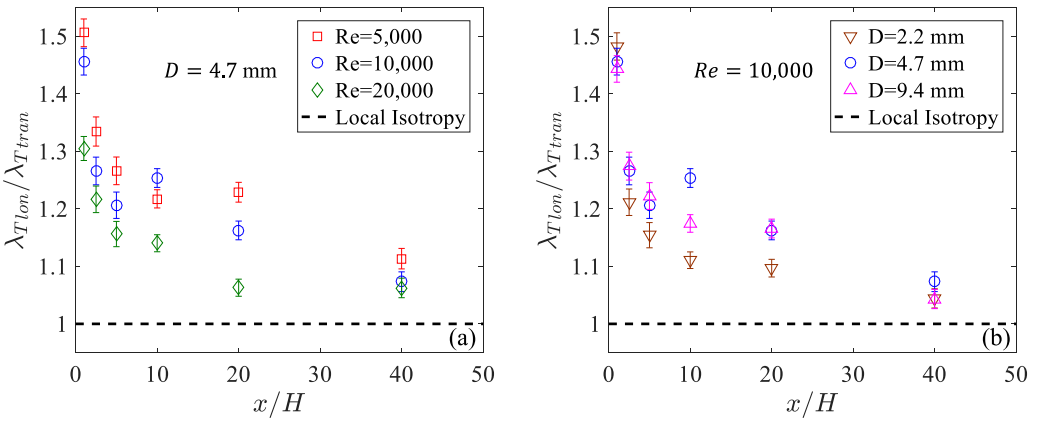

FIG. 8. Evolution of the ratio of longitudinal to transverse scalar Taylor microscales calculated from the spatial gradient of the concentration fluctuations as a function of (a) Reynolds number and (b) source nozzle diameter.

equal [49]. The ratio between longitudinal and transverse scalar Taylor microscales equals

$$\frac{\lambda_{T_{\text{lon}}}}{\lambda_{T_{\text{tran}}}} = \sqrt{\frac{\left\langle \left(\frac{\partial C'}{\partial y}\right)^2 \right\rangle}{\left\langle \left(\frac{\partial C'}{\partial x}\right)^2 \right\rangle}}, \tag{7}$$

which is also the ratio between the transverse and longitudinal components of the dissipation rate of the scalar fluctuations. This ratio decreases with downstream distance and is found to be between 1.1 and 1.2 in the self-similar regime ($x/H \geqslant 10$), which is similar to the reported typical values of 1.2 in the measurements of dissipation rate of the temperature fluctuations in a turbulent boundary layer by Sreenivasan *et al.* [50]. Also, Fig. 8 illustrates that the smallest ratio at each location occurs for the highest Reynolds number (Re = 20 000) and the smallest initial nozzle diameter ($D = 2.2$ mm), indicating these conditions achieve the greatest isotropy.

B. Fractal dimension of the scalar fluctuations

The other important question in the analysis of power spectra scaling is whether the scalar field has transitioned to the fully developed turbulent regime or not. The measure of fractality helps to answer this question and specifically is important for turbulent mixing, since the entrainment occurs through the interface of a turbulent region. Several studies show that it is possible to quantify the geometry of isosurfaces of the scalar field in terms of fractal dimension to investigate the range of scales in the scalar field, intermittency, and the critical fractal dimension for turbulence transition [51–57].

Dasi *et al.* [37] provided a thorough analysis of the fractal geometry for passive scalar fields. A similar box-counting algorithm is used in this study to analyze the fractal dimension of the concentration fluctuation fields. Figures 9(a)–9(c) and 9(g)–9(i) show the sample normalized concentration fluctuation fields for Re = 5000 at each location downstream, The corresponding level-set interfaces of the scalar fluctuation fields based on detection threshold of $C'_d/C_0 = 0.1$ are shown in Figs. 9(d)–9(f) and 9(j)–9(l). The results for fractal dimension do not vary significantly over a range of $0.1 < C'_d/C_0 < 0.4$.

The fractal dimension of the interface isocontour is evaluated using the box counting method [37,55]. In this method, the number of boxes required to cover a field (interface isocontour) is counted by applying several grids of decreasing size, and the details of the isocontour features can be investigated by the number of boxes containing a section of the isosurface for each grid size.

Figure 10(a) shows a sample coverage count plot, where the coverage count (N) decreases with normalized scale δ/δ_B, with a characteristic side scale of δ_B as the largest scale. The box sizes are successively subdivided into an increasing number of boxes of smaller size. Therefore, the consecutive box sizes are $\delta = 1024, 512, 256, 128, 64, 32, 16, 8, 4, 2$, and 1 pixels. Then, the box-counting dimension, F_D, of the fractal level set can be computed using

$$F_D = -\frac{d\log N_\delta}{d\log \delta}, \tag{8}$$

where N_δ is the number of boxes of the scale δ that is needed to cover the whole interface isocontour field. Figures 10(b) and 10(c) present the fractal dimension for the isocontours of the scalar fluctuation fields, examples of which are shown in Fig. 9. The results for the fractal dimension are in good agreement with the turbulent scalar length scales such that there is a change in the growth rate behavior of F_D around $x/H = 10$—the same distance where, according to the turbulent length scales, there is self-similar behavior in the flow. The fractal dimension increases from a low value near the source, in agreement with the findings of Mistry *et al.* [58] for axisymmetric jets. There is a sharp slow-down in the growth rate beyond $x/H = 10$, which is a sign of mixing transition in the flow. The change in the behavior of the fractal dimension in this study agrees well with the threshold value of $F_D = 1.36 \pm 0.05$ that was found for transitioning to a fully developed turbulent jet by Prasad and Sreenivasan [54]. This range of fractal dimension is highlighted with the green band

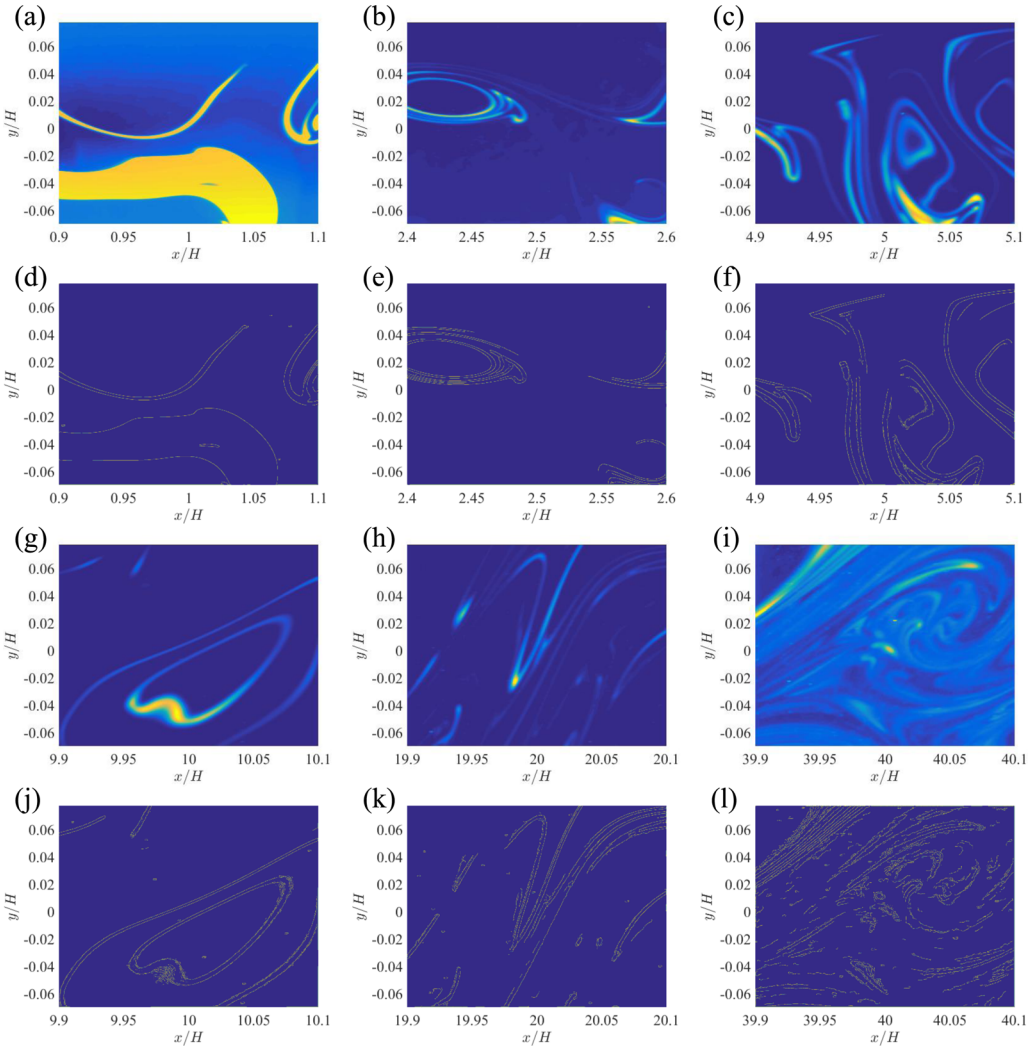

FIG. 9. Evolution of the sample normalized concentration fluctuation fields [(a), (b), (c), (g), (h), (i)] at different distances downstream, and their extracted isoconcentration contours [(d), (e), (f), (j), (k), (l)] for the detection threshold $C_d'/C_0 = 0.1$ for the case of Re $= 5\,000$ and $D = 4.7$ mm.

in Fig. 10. It is important to note that the fractal dimension of the isosurface of the concentration fluctuation increases at each location with increasing Reynolds number and initial release diameter. Overall, the results suggest that the fractal dimension of the scalar fluctuation fields, F_D, develops toward values between 1.3 and 1.5, and flow is transitioning to the fully developed regime at $x/H \geqslant 10$. The reported fractal dimension of the turbulent/nonturbulent interface in a boundary layer by de Silva *et al.* [59] and in an axisymmetric jet by Mistry *et al.* [60] ($F_D = 1.3 - 1.4$) is in good agreement with the current results.

C. Intermittency

The scalar intermittency factor is defined as the probability that the scalar value is above a threshold value [61], and it is computed as

$$\gamma = \text{prob}[C \geqslant C_T], \tag{9}$$

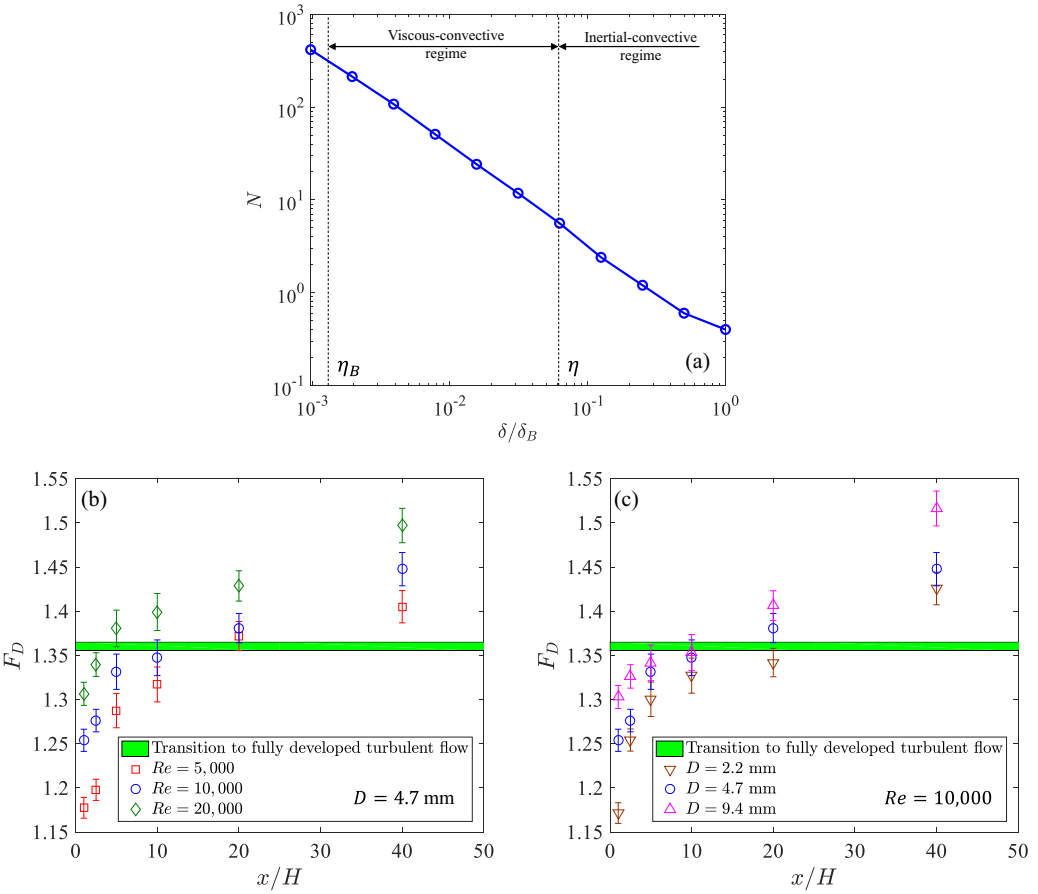

FIG. 10. (a) A sample log-log plot of the number N of square area elements ("boxes") of size δ versus normalized scale of δ/δ_B at $x/H = 40$ for $D = 4.7$ mm and Re $= 10\,000$. (b), (c) Evolution of the fractal dimension estimate for the isoconcentration contours extracted for the detection threshold of $C_d' = 0.1$ as a function of (b) Reynolds number and (c) source nozzle diameter. The green shaded region corresponds to the fractal dimension threshold that was found for transition to a fully developed turbulent jet by Prasad and Sreenivasan [54].

where $C_T = 0.0002C_0$ is the scalar threshold value that is chosen to be well above the experimental noise level. It should be noted that based on this definition, a steady scalar time record has a high intermittency factor close to 1, and a sporadic time record has a low-intermediate intermittency factor.

Figures 11(a) and 11(b) show the average value of the intermittency factor for the three Reynolds numbers and three injection length scales, respectively. The intermittency factor initially decreases, reaching a minimum value, followed by a gradual increase toward the value of 0.5–0.75. The intermittency factor increases with Reynolds number and injection length scale. Therefore, the scalar filaments are encountered more frequently at a point with increasing Reynolds number or injection length scale.

Figures 12 and 13 show the probability density functions (PDFs) of the fluctuations of the transverse concentration gradient, normalized by its standard deviation, at different Reynolds numbers and initial release diameters [10,49]. The non-Gaussian PDFs are consistent with the results of intermittency factor and reflect strong fluctuations. The length of the tails is remarkable,

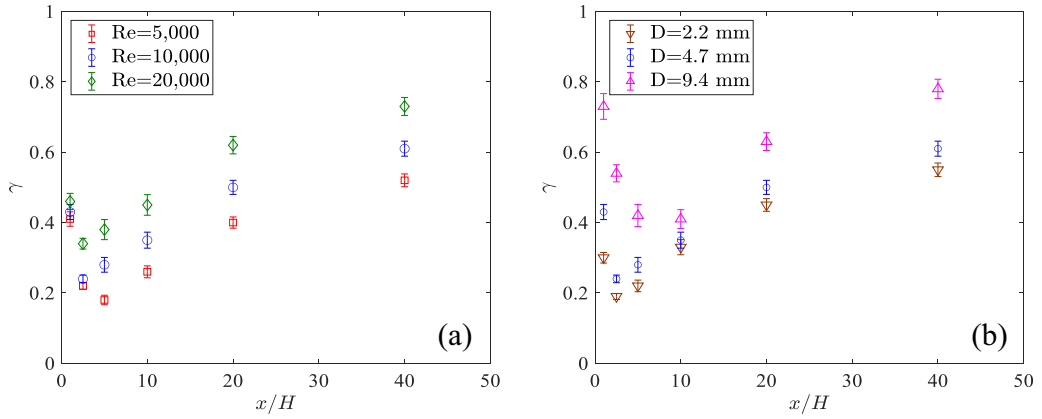

FIG. 11. Evolution of the average intermittency factor as a function of (a) Reynolds number and (b) nozzle diameter.

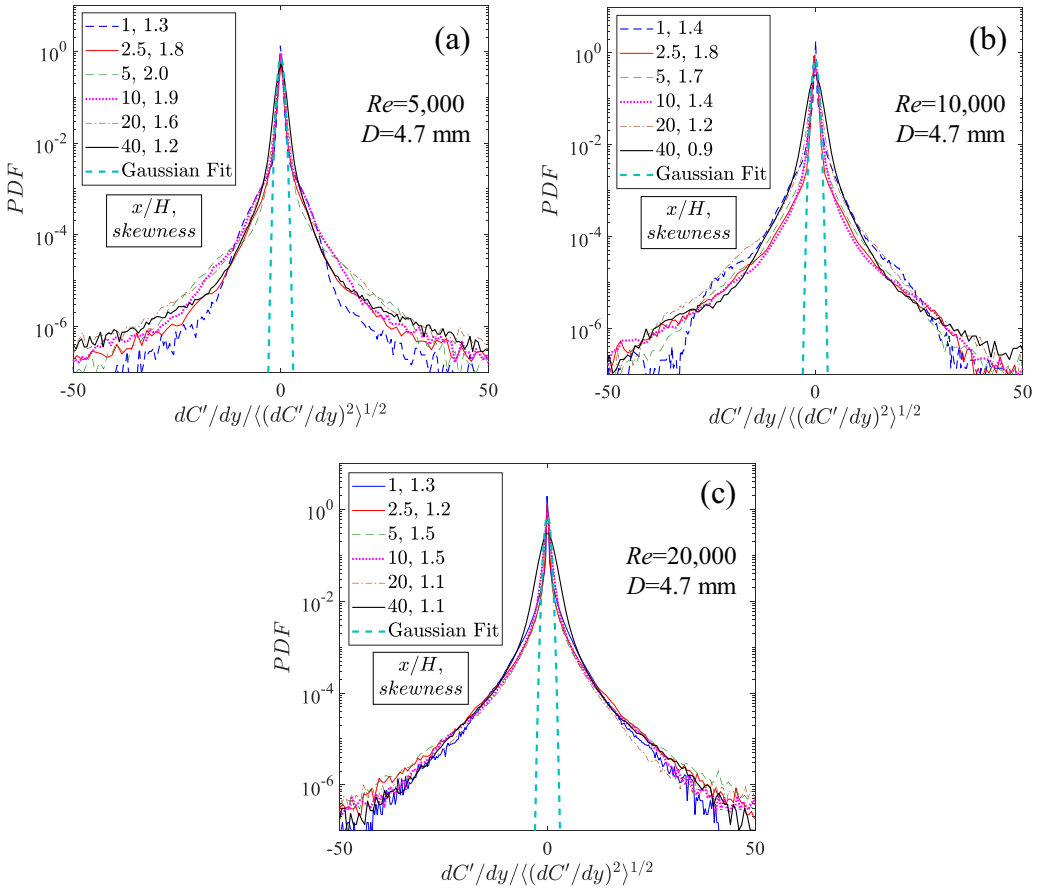

FIG. 12. PDF of the fluctuations of the transverse concentration gradient normalized by its standard deviation for (a) Re = 5 000, (b) Re = 10 000, and (c) Re = 20 000 while the source nozzle diameter is maintained at $D = 4.7$ mm. The legend reports the x/H location for each curve and the skewness of the PDF.

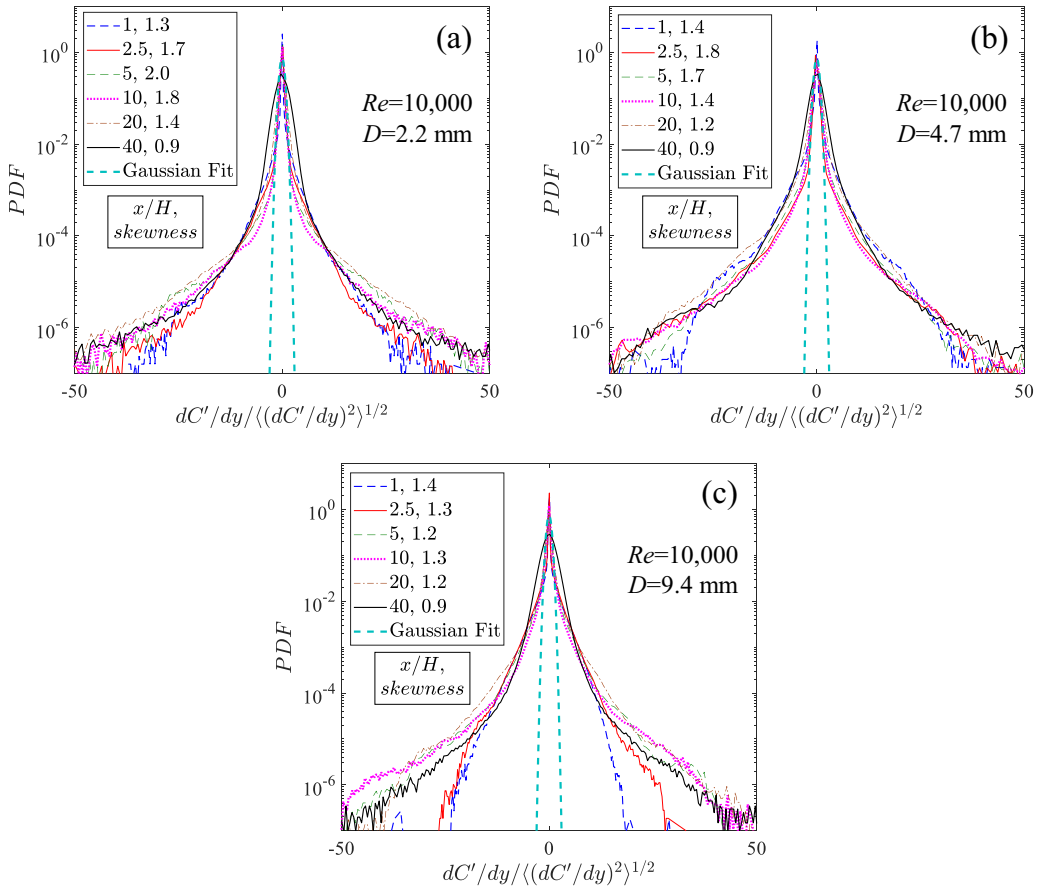

FIG. 13. PDF of the fluctuations of the transverse concentration gradient normalized by its standard deviation (a) $D = 2.2$ mm, (b) $D = 4.7$ mm, and (c) $D = 9.4$ mm while the Reynolds number is maintained at $\mathrm{Re} = 10\,000$. The legend reports the x/H location for each curve and the skewness of the PDF.

showing scalar gradients at the smallest scale with amplitudes up to ± 40 times the standard deviation, which is consistent with the small-scale intermittency of the concentration fluctuations. Increasing Reynolds number appears to spread the PDFs of the near source cases due to the presence of finer scales and steeper instantaneous scalar gradients. The PDFs farther downstream are relatively unaffected by an increase in Reynolds number. The PDFs for the near source cases suggest a significant effect of initial release diameter (Fig. 13). The range of fluctuations clearly decreases with increasing injection length scale depicted by the narrowing of the PDFs. In addition, the skewness of the PDFs is included for each case in Figs. 12 and 13. The slight asymmetry of the distributions is a well known property of small-scale persistence of anisotropy [10]. The skewness values are of O(1) and appear fairly constant with downstream distance. Therefore, an increase in Reynolds number does not appear to reduce the anisotropy of the scalar structure. The skewness values reported herein are greater than the values reported by Yeung *et al.* [13] for the case of high Schmidt number passive scalar mixing driven by a mean gradient in DNS simulations of a locally isotropic velocity field. This may indicate that the mean velocity gradient and other anisotropic characteristics of the velocity field also contribute to the small-scale anisotropy of the passive scalar structure.

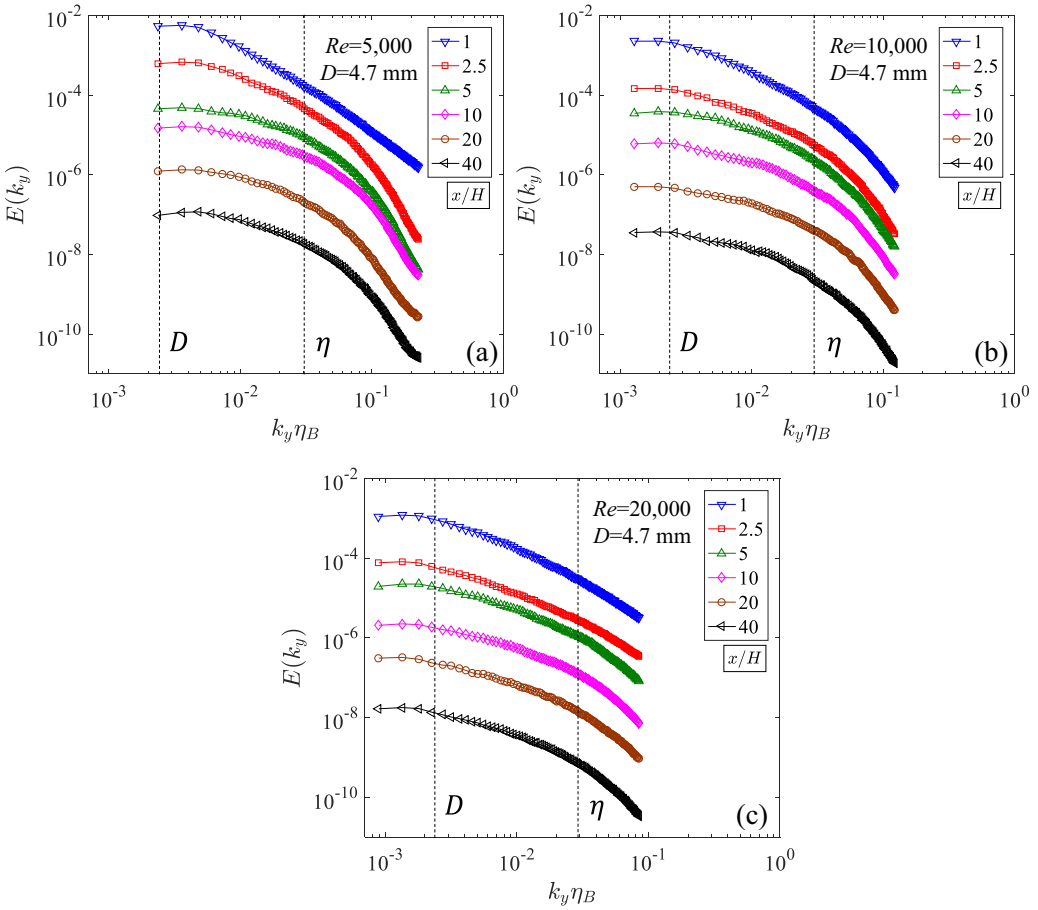

FIG. 14. Evolution of the transverse spectra of the fluctuating scalar field for (a) Re = 5 000, (b) Re = 10 000, and (c) Re = 20 000 while the source nozzle diameter is maintained at $D = 4.7$ mm.

D. Scalar power spectra

One of the most important results for the turbulent mixing of high Schmidt number passive scalars include the power spectrum characterization via scaling laws. With the assumption of local isotropy of the velocity field and the passive scalar field, the scaling laws were predicted to be proportional to $k^{-5/3}$ [1–3] and k^{-1} [6,7] in the inertial-convective and viscous-convective regimes, respectively. Here, the one-dimensional transverse spectrum, which characterizes the local structure of the passive scalar field, is examined for the different Reynolds numbers and injection length scales for all distances from the source. The transverse spectrum is examined because that direction is consistent with the strongest gradients in the mean velocity and scalar fields. The one-dimensional power spectrum is calculated by averaging the power spectra estimated for parallel one-dimensional spatial transects of the scalar fluctuation field, and then ensemble averaged for the entire dataset at each location. The power spectrum of each transect is estimated via standard algorithms following Mohaghar *et al.* [34,35]. A noise floor is identified in the averaged one-dimensional power spectrum and subtracted to generate the optimal (Weiner) filtered power spectrum estimate. The averaged power spectrum of the scalar field is calculated using

$$E(k_y) = FFT(C')\text{conj}[FFT(C')], \tag{10}$$

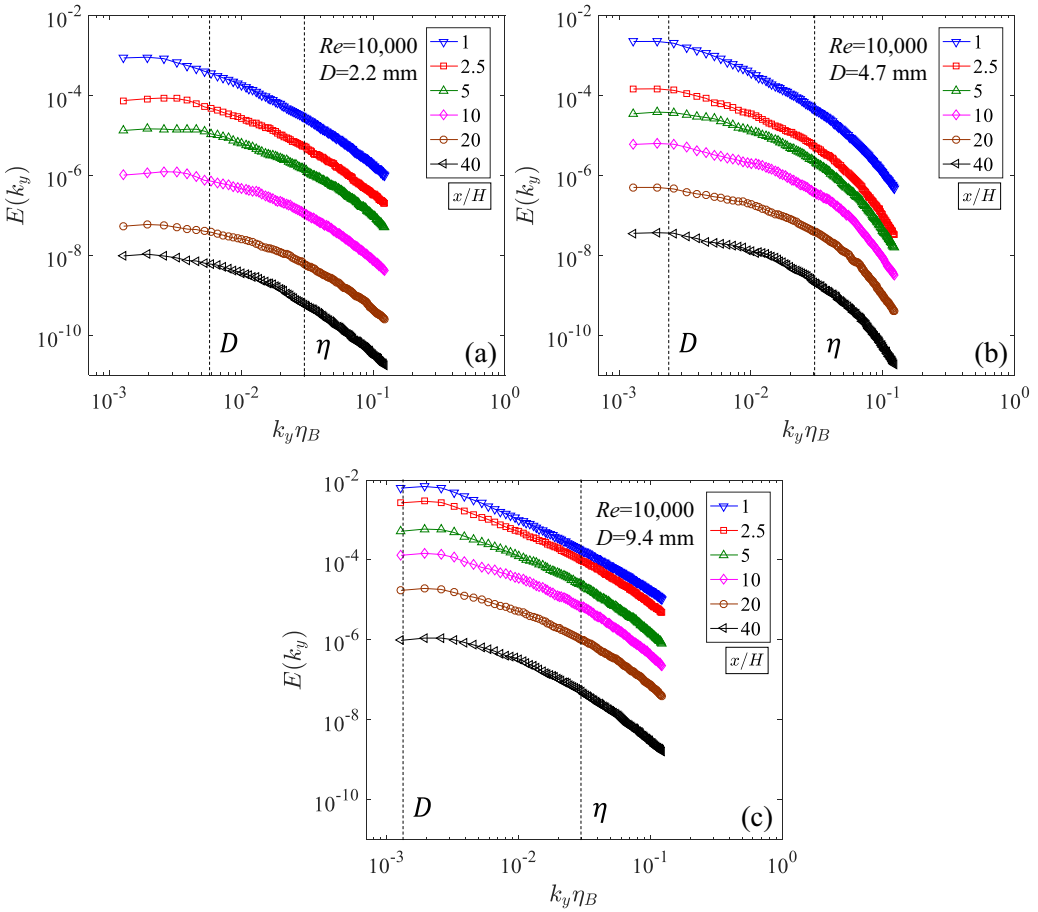

FIG. 15. Evolution of the transverse spectra of the fluctuating scalar field for (a) $D = 2.2$ mm, (b) $D = 4.7$ mm, and (c) $D = 9.4$ mm while the Reynolds number is maintained at Re $= 10\,000$.

where $FFT(C')$ is the Fourier transform of the 2π periodic function in the transverse direction and conj$[FFT(C')]$ is its complex conjugate.

Figures 14 and 15 show the one-dimensional transverse power spectra of the passive scalar field at six distances for the three Reynolds numbers and the three injection length scales, respectively. The horizontal axes are normalized by the Batchelor length scale (Table I). The normalized wave number corresponding to the Kolmogorov length scale, η_B/η, is of the order of $\mathrm{Sc}^{-1/2} \approx 3 \times 10^{-2}$ and is indicated in each figure. The wave number corresponding to the source injection size, D, is also shown on each of the plots. Each power spectrum shows evidence of scaling behavior in the inertial-convective regime. There is a slight transition around the wave number corresponding to the Kolmogorov length scale with the magnitude of the spectral slope increasing into and within the viscous-convective regime. The spectra have been cut off before the highest resolved wave number as the variance from random noise dominates the signal. The transition near the wave number corresponding to the Kolmogorov length scale is observed for all spectra calculated in the present study. The power spectra decreases with downstream distance for all three Reynolds numbers, and the magnitude at large scales decreases with increasing Reynolds number at each location (Fig. 14). The primary noticeable change in the spectra with respect to injection length scale is the increase in the overall power with increasing injection length scale. This is due to the increase in the magnitude of the concentration fluctuations with increasing injection length scale (Fig. 15).

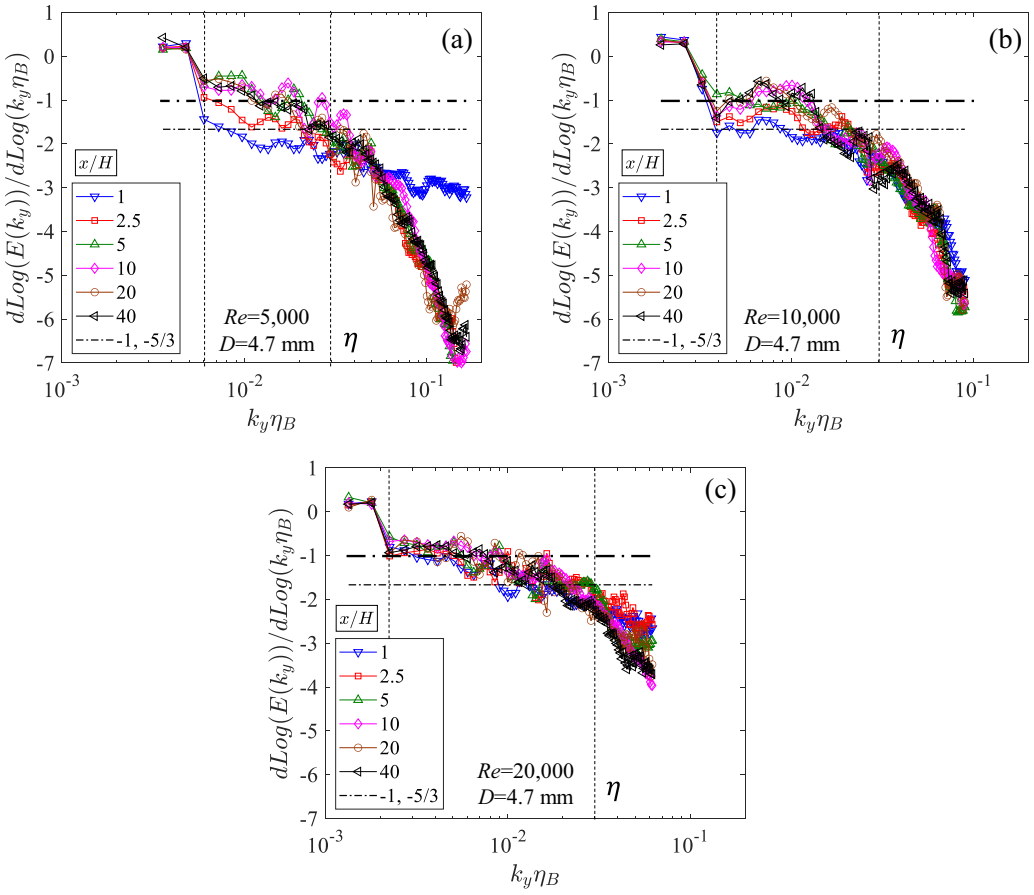

FIG. 16. Evolution of the logarithmic derivative of the transverse spectra of the fluctuating scalar field for (a) Re = 5 000, (b) Re = 10 000, and (c) Re = 20 000 while the source nozzle diameter is maintained at $D = 4.7$ mm. The horizontal dash-dotted lines correspond to k^{-1} and $k^{-5/3}$ scaling.

The quantitative comparison of the slope of the spectra is established by computing the logarithmic derivative (i.e., the slope on a log-log plot) of each spectra [19,62], which is defined by $d\{\log[E(k_y)]\}/d[\log(k_y\eta_B)]$. Figures 16 and 17 show the logarithmic derivative of the one-dimensional transverse spectra plotted in Figs. 14 and 15, respectively. The dash-dotted lines in the plots represent the -1 and $-5/3$ slope corresponding to the slope of the inertial-convective regime predicted by Villermaux *et al.* [63] for the cascade-bypass situation and by the Kolmogorov-Obukhov-Corrsin scaling, respectively. Villermaux *et al.* [63] introduced the "cascade-bypass" situation that arises when the scalar is released at a length scale within the inertial-convective regime. It was shown that the scalar spectrum bypasses the $k^{-5/3}$ scaling for wave numbers smaller than or close to the injection wave number in the inertial-convective regime and assumed a k^{-1} scaling due to the presence of a dominant stretching rate associated with the initial size of the scalar filament. In the current results, the magnitude of the spectral slope decreases with downstream distance for all cases until $x/H = 10$. The trend and magnitude is quite similar for $x/H \geqslant 10$, where turbulent scalar length scales suggest that self-similarity occurs in the scalar field. In this self-similar regime ($x/H \geqslant 10$), the scaling exponent of the smallest and the middle nozzle diameters ($D = 2.2$ and 4.7 mm) in the lower wave-number portion of the inertial-convective regime (i.e., lower wave numbers and larger scales), where the injection length scale is smaller than or close to the length

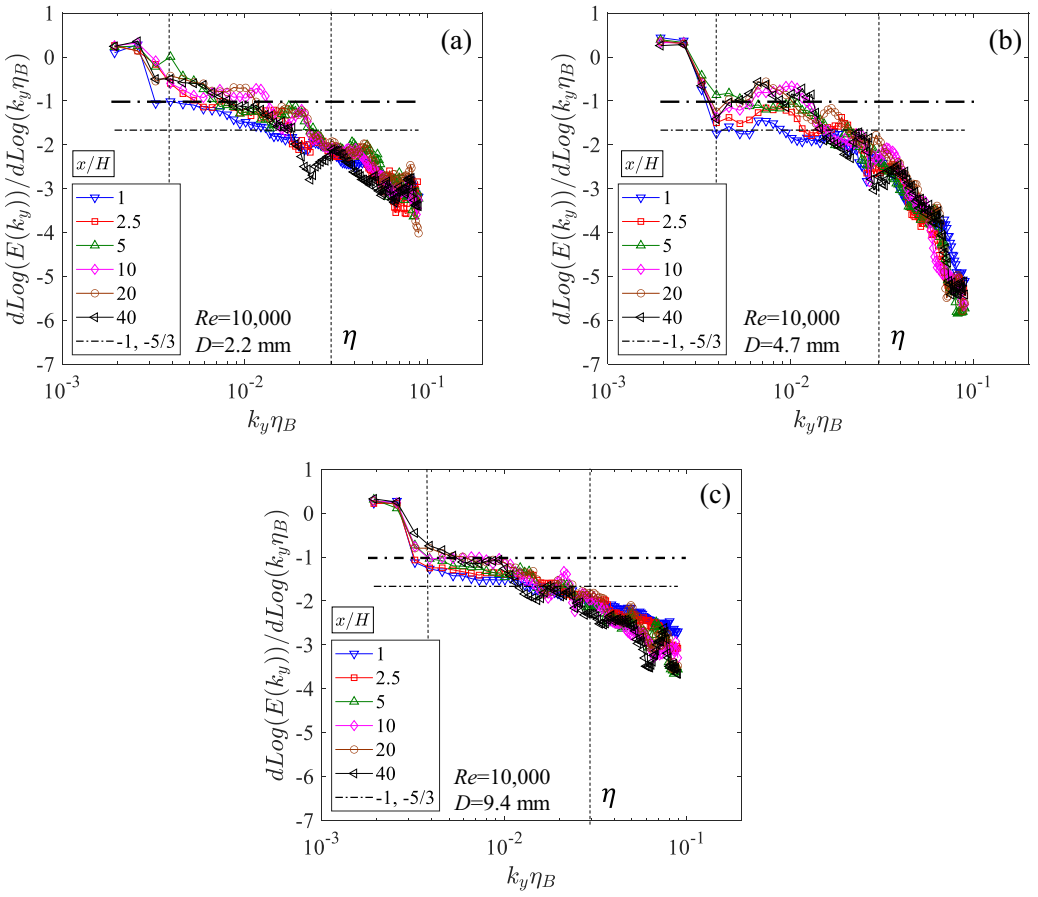

FIG. 17. Evolution of the logarithmic derivative of the transverse spectra of the fluctuating scalar field for (a) $D = 2.2$ mm, (b) $D = 4.7$ mm, and (c) $D = 9.4$ mm while the Reynolds number is maintained at $\mathrm{Re} = 10\,000$. The horizontal dash-dotted lines correspond to k^{-1} and $k^{-5/3}$ scaling.

scale of the fluctuating scalar field, is closer to k^{-1} scaling in agreement with the cascade-bypass situation. The ratio of D/η for each case is provided in Table I. For the largest nozzle diameter [$D = 9.4$ mm, Fig. 17(c)], where the wave number related to the nozzle diameter is outside of the inertial-convective regime, the magnitude of the spectral slope is slightly greater than other cases (between -1 and $-5/3$). The scaling exponent in the upper wave-number portion of the inertial-convective regime for all cases is closer to $k^{-5/3}$ scaling. The increase in the magnitude of the spectral slope for the near source cases is related to the mean scalar gradient [64]. The scalar variance is dissipated at lower wave numbers, i.e., larger scales, compared to farther downstream. This is consistent with the smaller fractal dimension near the source and a larger scalar Taylor microscale near the source.

Furthermore, the magnitude of the logarithmic derivatives shows no indication of a k^{-1} scaling behavior in the viscous-convective regime. It must be noted that although the spectral data are dominated by noise for about half of the viscous-convective regime, the data for the lower wave-number portion of the viscous-convective regime is sufficient to speculate on the existence of Batchelor's scaling. Also, the amount of time the scalar filaments are exposed to turbulence is greater than the Batchelor diffusion time, $t_B = t_\eta \ln(\mathrm{Sc})$ (i.e., the time required for scalar filaments to evolve from a thickness of η to η_B). For the three Reynolds numbers, the Batchelor diffusion time is 2.0,

0.6, and 0.3 s, whereas the travel times for the scalar to reach the first measurement location are 1.7, 0.8, and 0.4 s, respectively. Therefore, there has been sufficient time for filaments to be broken down to form an equilibrium in the viscous-convective regime, and if that equilibrium has been reached, theory would predict a k^{-1} scaling. However, the observations in Figs. 16 and 17 are in conflict with Batchelor's k^{-1} prediction. Further, the logarithmic derivatives in the viscous-convective regime (Figs. 16 and 17) decrease with respect to $k_y\eta_B$, in agreement with Miller and Dimotakis [19]. Although an increase in Reynolds number appears to increase the spectral slope, there is still a continuous decrease in the spectral slope in the viscous-convective regime at highest Reynolds number. This conflict between theory and observation for the scaling of the viscous-convective regime can be explained by the high intermittency in the small scales of the scalar fluctuations in the experimental results, which develops significant non-Gaussian tails in the PDF of the small-scale quantities (Figs. 12 and 13). This high intermittency in the small scales effectively produces large scalar dissipation rate, which affects the scaling of the viscous-convective regime.

IV. CONCLUSIONS

The present study addresses the characteristics of the high-Schmidt-number passive scalar fields resulting from an isokinetic release in a turbulent boundary layer by investigating the effects of Reynolds number and initial release diameter on turbulent scalar length scales, fractal geometry, intermittency, and power spectrum in the inertial-convective and viscous-convective regimes. The constant ratio between the scalar integral length scale and scalar Taylor microscale suggests that the flow reaches a self-similar regime for locations exceeding $x/H \geqslant 10$. Another indication of self-similarity is that all turbulence quantities approach a constant asymptotic value for those locations. In addition, the ratio between the longitudinal and transverse scalar Taylor microscales indicates that the flow is approaching local isotropy in the self-similar regime and the value is close to 1.1–1.2, which is in agreement with the findings of Sreenivasan *et al.* [50] for measurements of temperature fluctuations in a turbulent boundary layer.

A transition in the growth rate of the fractal dimension of the level sets of the concentration fluctuation fields is observed at the same locations that the scalar length scales showed self-similarity in the flow ($x/H \geqslant 10$). The fractal dimension value between 1.3 and 1.5 in this region is close to the ones reported for fractal dimension of interfaces in fully-developed turbulent flows [54].

The scaling-exponent in the inertial-convective regime of the power spectra is found to be dependent on initial release diameter in agreement with Villermaux *et al.* [63]. The effect of initial conditions was evident when the size of the nozzle diameter was in the range of inertial-convective regime. The exponent for the scales larger than or close to the initial release diameter (i.e., the lower wave-number portion of the inertial-convective regime), deviated from $-5/3$ and showed smaller values that were closer to k^{-1} scaling far downstream where the effects of large-scale anisotropy were minimal ($x/H \geqslant 10$). The spectral slope was closer to $-5/3$ for the upper wave-number portion of the inertial-convective regime. This observation is consistent with the cascade-bypass scenario suggested by Villermaux *et al.* [63]. In addition, the magnitude of scaling exponent near the source ($x/H < 10$) is larger due to the large-scale anisotropy.

The viscous-convective scaling behavior deviated significantly from Batchelor's k^{-1} scaling law for all Reynolds numbers and initial nozzle diameters, clearly disputing the generality of Batchelor's arguments. The observations agreed with the scaling behavior in Miller and Dimotakis [19] where a log-normal spectral decrease was observed. The analysis of intermittency factor and PDFs of the fluctuating scalar gradient suggest strong intermittency at the small scales of the scalar fluctuations. This significant intermittency, which generates non-Gaussian tails in the PDFs of the scalar fluctuations and produces large dissipation rate, explains the steep spectral slope in the viscous-convective regime.

ACKNOWLEDGMENT

The authors gratefully acknowledge the financial support of the National Science Foundation (CTS-0303406) and the Karen and John Huff Chair endowment.

[1] A. M. Oboukhov, Structure of the temperature field in turbulent flows, Isv. Geogr. Geophys. Ser. **13**, 58 (1949).
[2] S. Corrsin, On the spectrum of isotropic temperature fluctuations in an isotropic turbulence, J. Appl. Phys. **22**, 469 (1951).
[3] A. S. Monin and A. M. Yaglom, *Statistical Fluid Mechanics* (MIT Press, Cambridge, MA, 1975), Vol. 2.
[4] C. H. Gibson, Kolmogorov similarity hypotheses for scalar fields: Sampling intermittent turbulent mixing in the ocean and galaxy, Proc. R. Soc. London A **434**, 149 (1991).
[5] A. N. Kolmogorov, The local structure of turbulence in incompressible viscous fluid for very large reynolds numbers, Dolk. Akad. Nauk SSSR **30**, 301 (1941).
[6] G. K. Batchelor, Small-scale variation of convected quantities like temperature in turbulent fluid Part 1. General discussion and the case of small conductivity, J. Fluid Mech. **5**, 113 (1959).
[7] G. K. Batchelor, I. D. Howells, and A. A. Townsend, Small-scale variation of convected quantities like temperature in turbulent fluid Part 2. The case of large conductivity, J. Fluid Mech. **5**, 134 (1959).
[8] R. H. Kraichnan, Small-scale structure of a scalar field convected by turbulence, Phys. Fluids **11**, 945 (1968).
[9] K. R. Sreenivasan, The passive scalar spectrum and the Obukhov–Corrsin constant, Phys. Fluids **8**, 189 (1996).
[10] Z. Warhaft, Passive scalars in turbulent flows, Annu. Rev. Fluid Mech. **32**, 203 (2000).
[11] Jayesh, C. Tong, and Z. Warhaft, On temperature spectra in grid turbulence, Phys. Fluids **6**, 306 (1994).
[12] L. Mydlarski and Z. Warhaft, Passive scalar statistics in high-Péclet-number grid turbulence, J. Fluid Mech. **358**, 135 (1998).
[13] P. K. Yeung, S. Xu, and K. R. Sreenivasan, Schmidt number effects on turbulent transport with uniform mean scalar gradient, Phys. Fluids **14**, 4178 (2002).
[14] S. L. Tang, R. A. Antonia, L. Djenidi, L. Danaila, and Y. Zhou, Finite Reynolds number effect on the scaling range behavior of turbulent longitudinal velocity structure functions, J. Fluid Mech. **820**, 341 (2017).
[15] C. H. Gibson and W. H. Schwarz, The universal equilibrium spectra of turbulent velocity and scalar fields, J. Fluid Mech. **16**, 365 (1963).
[16] H. L. Grant, B. A. Hughes, W. M. Vogel, and A. Moilliet, The spectrum of temperature fluctuations in turbulent flow, J. Fluid Mech. **34**, 423 (1968).
[17] A. E. Gargett, Evolution of scalar spectra with the decay of turbulence in a stratified fluid, J. Fluid Mech. **159**, 379 (1985).
[18] S. Komori, T. Kanzaki, Y. Murakami, and H. Ueda, Simultaneous measurements of instantaneous concentrations of two species being mixed in a turbulent flow by using a combined laser-induced fluorescence and laser-scattering technique, Phys. Fluids A **1**, 349 (1989).
[19] P. L. Miller and P. E. Dimotakis, Measurements of scalar power spectra in high Schmidt number turbulent jets, J. Fluid Mech. **308**, 129 (1996).
[20] B. S. Williams, D. Marteau, and J. P. Gollub, Mixing of a passive scalar in magnetically forced two-dimensional turbulence, Phys. Fluids **9**, 2061 (1997).
[21] M. Holzer and E. D. Siggia, Turbulent mixing of a passive scalar, Phys. Fluids **6**, 1820 (1994).
[22] W. K. George, Self-preservation of temperature fluctuations in isotropic turbulence, in *Studies in Turbulence* (Springer, Berlin, 1992), pp. 514–528.
[23] G. Comte-Bellot and S. Corrsin, Simple Eulerian time correlation of full- and narrow-band velocity signals in grid-generated, "isotropic" turbulence, J. Fluid Mech. **48**, 273 (1971).

[24] Z. Warhaft and J. L. Lumley, An experimental study of the decay of temperature fluctuations in grid-generated turbulence, J. Fluid Mech. **88**, 659 (1978).
[25] R. M. R. Taveira, C. B. da Silva, and J. C. F. Pereira, The dynamics of turbulent scalar mixing near the edge of a shear layer, in *Journal of Physics: Conference Series* (IOP Publishing, Bristol, England, 2011), Vol. 318, p. 052049.
[26] C. Bahri, G. Arwatz, W. K. George, M. E. Mueller, and M. Hultmark, Self-similarity of passive scalar flow in grid turbulence with a mean cross-stream gradient, J. Fluid Mech. **780**, 215 (2015).
[27] G. Comte-Bellot and S. Corrsin, The use of a contraction to improve the isotropy of grid-generated turbulence, J. Fluid Mech. **25**, 657 (1966).
[28] A. Sirivat and Z. Warhaft, The effect of a passive cross-stream temperature gradient on the evolution of temperature variance and heat flux in grid turbulence, J. Fluid Mech. **128**, 323 (1983).
[29] M. R. Overholt and S. B. Pope, Direct numerical simulation of a passive scalar with imposed mean gradient in isotropic turbulence, Phys. Fluids **8**, 3128 (1996).
[30] G. J. Van Fossen and C. Y. Ching, Measurements of the influence of integral length scale on stagnation region heat transfer, Int. J. Rotat. Mach. **3**, 117 (1997).
[31] H. Wang and W. K. George, The integral scale in homogeneous isotropic turbulence, J. Fluid Mech. **459**, 429 (2002).
[32] P. L. O'Neill, D. Nicolaides, D. Honnery, and J. Soria, Autocorrelation functions and the determination of integral length with reference to experimental and numerical data, in *Proceedings of the 15th Australasian Fluid Mechanics Conference* (University of Sydney, NSW, Australia, 2004), Vol. 1, pp. 1–4.
[33] D. A. Donzis, K. R. Sreenivasan, and P. K. Yeung, Scalar dissipation rate and dissipative anomaly in isotropic turbulence, J. Fluid Mech. **532**, 199 (2005).
[34] M. Mohaghar, J. Carter, B. Musci, D. Reilly, J. McFarland, and D. Ranjan, Evaluation of turbulent mixing transition in a shock-driven variable-density flow, J. Fluid Mech. **831**, 779 (2017).
[35] M. Mohaghar, J. Carter, G. Pathikonda, and D. Ranjan, The transition to turbulence in shock-driven mixing: Effects of Mach number and initial conditions, J. Fluid Mech. **871**, 595 (2019).
[36] K. M. Talluru, J. Philip, and K. A. Chauhan, Self-similar spectra of point-source scalar plumes in a turbulent boundary layer, J. Fluid Mech. **870**, 698 (2019).
[37] L. P. Dasi, F. Schuerg, and D. R. Webster, The geometric properties of high-schmidt-number passive scalar isosurfaces in turbulent boundary layers, J. Fluid Mech. **588**, 253 (2007).
[38] L. P. Dasi, The small-scale structure of passive scalar mixing in turbulent boundary layers, Ph.D. thesis, Georgia Institute of Technology (2004).
[39] S. B. Pope, *Turbulent Flows* (Cambridge University Press, Cambridge, UK, 2000).
[40] G. K. Batchelor, *The Theory of Homogeneous Turbulence* (Cambridge University Press, Cambridge, UK, 1953).
[41] H. Tennekes, J. L. Lumley, and J. L. Lumley, *A First Course in Turbulence* (MIT Press, Cambridge, MA, 1972).
[42] D. R. Webster, S. Rahman, and L. P. Dasi, Laser-induced fluorescence measurements of a turbulent plume, J. Eng. Mech. **129**, 1130 (2003).
[43] S. Rahman and D. R. Webster, The effect of bed roughness on scalar fluctuations in turbulent boundary layers, Exp. Fluids **38**, 372 (2005).
[44] H. B. Fischer, J. E. List, C. R. Koh, J. Imberger, and N. H. Brooks, *Mixing in Inland and Coastal Waters* (Academic Press, San Diego, CA, 1979).
[45] J. O. Hinze, *Turbulence* (McGraw-Hill, New York, 1975).
[46] P. Huq and R. E. Britter, Mixing due to grid-generated turbulence of a two-layer scalar profile, J. Fluid Mech. **285**, 17 (1995).
[47] D. Aronson and L. Löfdahl, The plane wake of a cylinder: Measurements and inferences on turbulence modeling, Phys. Fluids A **5**, 1433 (1993).
[48] J. Ristorcelli and T. Clark, Rayleigh–Taylor turbulence: self-similar analysis and direct numerical simulations, J. Fluid Mech. **507**, 213 (2004).
[49] K. R. Sreenivasan, On local isotropy of passive scalars in turbulent shear flows, Proc. R. Soc. London A **434**, 165 (1991).

[50] K. R. Sreenivasan, R. A. Antonia, and H. Q. Danh, Temperature dissipation fluctuations in a turbulent boundary layer, Phys. Fluids **20**, 1238 (1977).
[51] B. B. Mandelbrot, *The Fractal Geometry of Nature* (WH Freeman, New York, 1983), Vol. 173.
[52] H. J. Catrakis and P. E. Dimotakis, Shape Complexity in Turbulence, Phys. Rev. Lett. **80**, 968 (1998).
[53] K. R. Sreenivasan and C. Meneveau, The fractal facets of turbulence, J. Fluid Mech. **173**, 357 (1986).
[54] R. R. Prasad and K. R. Sreenivasan, The measurement and interpretation of fractal dimensions of the scalar interface in turbulent flows, Phys. Fluids A **2**, 792 (1990).
[55] K. R. Sreenivasan, Fractals and multifractals in fluid turbulence, Annu. Rev. Fluid Mech. **23**, 539 (1991).
[56] P. Constantin, I. Procaccia, and K. R. Sreenivasan, Fractal Geometry of Isoscalar Surfaces in Turbulence: Theory and Experiments, Phys. Rev. Lett. **67**, 1739 (1991).
[57] P. Flohr and D. Olivari, Fractal and multifractal characteristics of a scalar dispersed in a turbulent jet, Physica D: Nonlin. Phenom. **76**, 278 (1994).
[58] D. Mistry, J. R. Dawson, and A. R. Kerstein, The multi-scale geometry of the near field in an axisymmetric jet, J. Fluid Mech. **838**, 501 (2018).
[59] C. M. de Silva, J. Philip, K. Chauhan, C. Meneveau, and I. Marusic, Multiscale Geometry and Scaling of the Turbulent-Nonturbulent Interface in High Reynolds Number Boundary Layers, Phys. Rev. Lett. **111**, 044501 (2013).
[60] D. Mistry, J. Philip, J. R. Dawson, and I. Marusic, Entrainment at multi-scales across the turbulent/nonturbulent interface in an axisymmetric jet, J. Fluid Mech. **802**, 690 (2016).
[61] P. C. Chatwin and P. J. Sullivan, The intermittency factor of scalars in turbulence, Phys. Fluids A **1**, 761 (1989).
[62] A. R. Kerstein, Linear-eddy modeling of turbulent transport. Part 6. Microstructure of diffusive scalar mixing fields, J. Fluid Mech. **231**, 361 (1991).
[63] E. Villermaux, C. Innocenti, and J. Duplat, Short circuits in the Corrsin–Obukhov cascade, Phys. Fluids **13**, 284 (2001).
[64] D. R. Dowling and P. E. Dimotakis, Similarity of the concentration field of gas-phase turbulent jets, J. Fluid Mech. **218**, 109 (1990).